

Effect of seed layers on the static and dynamic magnetic properties of CoIr films with negative effective magnetocrystalline anisotropy

Tianyong Ma(马天勇), Sha Zhang(张莎), Chenhu Zhang(张晨虎), Zhiwei Li(李志伟), Tao Wang(王涛), and Fashen Li(李发伸)

Citation: Chin. Phys. B, 2023, 32 (**12**): 127503. DOI: 10.1088/1674-1056/acd523
Journal homepage: http://cpb.iphy.ac.cn; http://iopscience.iop.org/cpb

What follows is a list of articles you may be interested in

Tuning magneto-dielectric properties of Co_2Z ferrites via Gd doping for high-frequency applications

Jian Wu(武剑), Bing Lu(卢冰), Ying Zhang(张颖), Yixin Chen(陈一鑫), Kai Sun(孙凯), Daming Chen(陈大明), Qiang Li(李强), Yingli Liu(刘颖力), and Jie Li(李颉)
Chin. Phys. B, 2023, 32 (**9**): 097501. DOI: 10.1088/1674-1056/acc3f7

Electric-field control of perpendicular magnetic anisotropy by resistive switching via electrochemical metallization

Yuan Yuan(袁源), Lu-Jun Wei(魏陆军), Yu Lu(卢羽), Ruo-Bai Liu(刘若柏), Tian-Yu Liu(刘天宇), Jia-Rui Chen(陈家瑞), Biao You(游彪), Wei Zhang(张维), Di Wu(吴镝), and Jun Du(杜军)
Chin. Phys. B, 2023, 32 (**6**): 067505. DOI: 10.1088/1674-1056/acbde8

Gate-voltage control of alternating-current-driven skyrmion propagation in ferromagnetic nanotrack devices

Xin-Yi Cai(蔡心怡), Zhi-Hua Chen(陈志华), Hang-Xiao Yang(杨航霄), Xin-Yan He(何鑫岩), Zhen-Zhen Chen(陈珍珍), Ming-Min Zhu(朱明敏), Yang Qiu(邱阳), Guo-Liang Yu(郁国良), and Hao-Miao Zhou(周浩淼)
Chin. Phys. B, 2023, 32 (**6**): 067502. DOI: 10.1088/1674-1056/acb420

Prediction of $LiCrTe_2$ monolayer as a half-metallic ferromagnet with a high Curie temperature

Li-Man Xiao(肖丽蔓), Huan-Cheng Yang(杨焕成), and Zhong-Yi Lu(卢仲毅)
Chin. Phys. B, 2023, 32 (**5**): 057505. DOI: 10.1088/1674-1056/acbe2e

Bending sensor based on flexible spin valve

L I Naumova, R S Zavornitsyn, M A Milyaev, N G Bebenin, A Y Pavlova, M V Makarova, I K Maksimova, V V Proglyado, A A Zakharov, and V V Ustinov
Chin. Phys. B, 2023, 32 (**5**): 057502. DOI: 10.1088/1674-1056/ac8923

Effect of seed layers on the static and dynamic magnetic properties of CoIr films with negative effective magnetocrystalline anisotropy

Tianyong Ma(马天勇)[1], Sha Zhang(张莎)[1], Chenhu Zhang(张晨虎)[2], Zhiwei Li(李志伟)[2], Tao Wang(王涛)[2,†], and Fashen Li(李发伸)[2]

[1] *The Key Laboratory of Physics and Photoelectric Information Functional Materials, North Minzu University, Yinchuan* 750021, *China*
[2] *Key Laboratory for Magnetism and Magnetic Materials of the Ministry of Education, Lanzhou University, Lanzhou* 730000, *China*

(Received 5 December 2022; revised manuscript received 28 April 2023; accepted manuscript online 12 May 2023)

The *c*-axis oriented hcp-$Co_{81}Ir_{19}$ magnetic films were prepared on different seed layers (Ni, Cu, Ir, Pt, Au, and No seed). We systematically investigated the impact that surface-free energy and strain energy have on the orientation and defects and/or internal stress of the grains by increasing the lattice mismatch ratio. Moreover, the initial permeability and the natural resonance frequency were discussed in great detail using a comparison between calculated values and experimental values. We found that the almost unchanged $4\pi M_s$ and μ_i are not affected, while the changed H_c, intrinsic K_{grain}, and f_r are strongly dependent on the seed layer and seed layer material. Moreover, the extracted damping constant is sensitive to the defects and/or internal stress and orientation of the grains. Therefore, the soft magnetic properties and microwave properties are adjusted and optimized by seed layers with different materials.

Keywords: seed layers, magnetic anisotropy, surface free energy, soft magnetic thin films

PACS: 77.55.Px, 75.30.Gw, 34.20.–b, 75.70.–i **DOI:** 10.1088/1674-1056/acd523

1. Introduction

Soft magnetic thin films (SMTFs) are widely investigated and highly desired for practical applications, such as microwave absorbers, inductors, micro-transformers, exchange-coupled composite media, and near field electromagnetic noise absorbers.[1,2] In practical application, SMTFs have to possess the basic demands including high saturation magnetization M_s, low coercivity H_c, high permeability, and high natural resonance frequency (f_r) as far as possible. Fe- and Co-based soft magnetic films exhibit excellent saturation magnetization, low coercivity, and high electrical resistivity.[3,4] Their microwave properties are governed by the following equation in the bian-isotropy model:[5]

$$\mu_i = 1 + \frac{4\pi M_s}{H_u} \quad f_r = \frac{\gamma}{2\pi}\sqrt{H_u\left(4\pi M_s - H_{grain}\right)}, \qquad (1)$$

where μ_i and f_r are the initial permeability and the natural resonance frequency, respectively. γ is the gyromagnetic ratio. $H_{grain} = 2K_{grain}/M_s$ is the effective magnetocrystalline anisotropy field with the corresponding magnetocrystalline anisotropy constant K_{grain}. According to our previous work,[6] oriented hcp-CoIr SMTFs with a certain Ir content have the effective negative magnetocrystalline anisotropy. It is clear that negative K_{grain} can increase f_r without affecting μ_i from Eq. (1). Moreover, magnetic moments are strictly restricted in the film plane by negative magnetocrystalline anisotropy. So, the oriented hcp-CoIr film can have sufficient thickness to obtain enough magnetic flux signal in practical uses of magnetic devices.

The metal seed layers between the substrate and the magnetic film, such as Ta/Pt/Ru, Ti/Au, and Ta/Ru, have made a highly oriented hcp-CoIr film.[6,7] The higher oriented texture of CoIr films has a smaller negative magnetocrystalline anisotropy as the Cu or Cu/Ru seed layers can increase the perpendicular magnetic anisotropy of $Co_{80}Pt_{20}$ films.[8] Moreover, good soft magnetic properties have also been obtained, namely, the seed layer is effective to reduce H_c without affecting M_s. Studies have reported that Co, Cu, and Ru seed layers make FeCo films magnetically softer.[9] Simultaneously, the high-frequency properties determined by the static magnetic parameters are also improved by using a seed layer, such as $Fe_{65}Co_{35}$ thin films with Ru and Rh seed layers.[10] In high-frequency practical applications, the magnetic damping constant α is also a key parameter and varies a bit with the choice of seed layer.[10] With the extrinsic contribution, the lower α value is associated with less magnetic inhomogeneities.[11] And the intrinsic contribution is relative to fundamental properties such as M_s.[12] In other words, epitaxial growth induced by a seed layer is the most efficient method to form a higher orientation and make the films magnetically softer and to improve high-frequency properties.

CoIr grains with strong negative magnetocrystalline anisotropy have an hcp structure. As mentioned above, the hcp-Ru (002) and fcc-Au (111) seed layers were used to induce the *c*-axis orientation of CoIr grains. Although the fcc-(111) plane of Ni, Cu, Ir, and Pt is similar to the hcp-(002) plane of CoIr, the seed layers of these metals have not been studied for CoIr SMTFs. Moreover, lattice mismatch ratios

†Corresponding author. E-mail: wtao@lzu.edu.cn

© 2023 Chinese Physical Society and IOP Publishing Ltd

have a tremendous influence on the crystallographic quality of epitaxial thin films[13,14] (e.g., magnetic film's stress state and texture formation). Therefore, in order to investigate and understand the effects of other material seed layers and lattice mismatch ratios on the CoIr magnetic layer, we used the fcc-(111) Ni, Cu, Ir, Pt, and Au seed layers to induce the oriented hcp-CoIr thin films with the *c*-axis of grains perpendicular to the film plane. We studied the effects of different seed layers on microstructure, soft magnetic properties, and negative effective magnetocrystalline anisotropy. Besides the static magnetic properties, dynamic studies were performed using field sweep ferromagnetic resonance (FMR) measurements and the damping constant affected by seed layers was studied through a vector network analyzer (VNA).

2. Experiment

All magnetic thin films studied in this work were prepared by the DC magnetron sputtering technique, which is similar to our earlier work with a layered structure of substrate/Ti/*M*/CoIr (*M* = Ni, Cu, Ir, Pt, Au, none) as shown in Fig. 1(a). A Si wafer with surface oxidation was used as the substrate, and the amorphous Ti layer (8 nm) was deposited on the substrate in order to provide a clean and flat surface. The oriented seed layer *M* (Ni, Cu, Ir, Pt, Au) of about 25 nm was grown on the Ti layer to help the CoIr magnetic layer reach about 50 nm. Compared with other films, the film was fabricated without a seed layer between the Ti layer and the magnetic layer. When fabricating the Ti and seed layers, purity Ar was used as the sputtering working gas at a pressure of 0.25 Pa. Then under the condition of 0.3 Pa purity Ar, CoIr magnetic layers were sputter deposited using a Co target with five Ir chips symmetrically placed on the Co target. About 10 cm away from the targets, the substrates were mounted on the center of the sample turntable. Chemical composition has been characterized by energy dispersive spectrometry (EDS). The crystalline structures were studied using the x-ray diffraction technique (XRD). The morphologies were observed by transmission electron microscopy (TEM). The static magnetic properties were measured with a vibrating sample magnetometer (VSM). Total out-of-plane anisotropy fields and the effective negative magnetocrystalline anisotropy were thoroughly investigated by electron spin resonance measurements (ESR). The damping constants for all films were thoroughly investigated by a VNA.

3. Results and discussion

Schematic diagrams of the hcp-CoIr (002) plane and fcc-*M* (111) plane are shown in Fig. 1(b). Half of the regular hexagon is seen on both the hcp-CoIr (002) plane and the fcc-*M* (111) plane, suggesting that lattice mismatches come from the difference in inter-atomic distance. The inter-atomic distances of fcc-(111) Ni, Cu, Ir, Pt, and Au are 2.49 Å, 2.55 Å, 2.72 Å, 2.77 Å, and 2.88 Å, respectively. The lattice mismatch ratios are about −0.81%, 1.59%, 8.37%, 10.36%, and 14.74% for the lattice spacing of hcp-Co (002) of ∼ 2.51 Å.

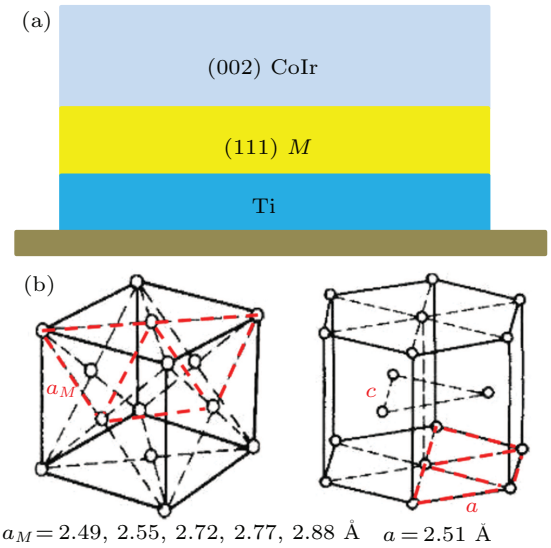


Fig. 1. (a) Schematic of the layer structure of our samples. (b) The crystal structures of fcc-(111) Ni, Cu, Ir, Pt, Au, and hcp-CoIr(002), half of the regular hexagon on *M* (111) plane and CoIr (002) plane are marked with red dotted lines.

XRD patterns of the samples measured with a θ–2θscan are shown in Fig. 2(a). Only two diffraction peaks corresponding to the *M* (111) plane and the CoIr (002) plane can be seen. For the sample without a seed layer, only CoIr (002) has a diffraction peak. Obviously, the intensity of the *M* (111) peak gradually increases and the position shifts to low 2θ because of the enlargement of the lattice parameters from Ni to Au. With the lattice mismatch ratio, the positions of the CoIr (002) peak show no obvious changes, and the intensity first showed small changes, then rapidly became strong and sharp. However, for the film without a seed layer, there is a significant right drift of the CoIr (002) peak, which indicates that the lattice constant of the CoIr phase becomes small. The smaller lattice constant results from the decreasing number of Ir atoms successfully entering the crystal structure of hcp-(CoIr). Meanwhile, the CoIr (002) peak gets broader and its intensity becomes weaker. Therefore, the films with a seed layer are more textured along the *c*-axis alignment than the film without a seed layer. And the degree of orientation improved by increasing the lattice mismatch ratio. However, the intensity of the CoIr (002) peak for the Au seed layer film is about 11 times that of the Ni seed layer film, which is inexplicable. As shown in Fig. 2(b), we plot the crystal *c* lattice parameter and FWHM determined from the profile fit to the CoIr (002) peak. One can see that *c* shows little change with the exception of the first one. The mean value of 0.4125 nm is about 0.13% larger than that of the first *c* parameter, which has been explained previously. Moreover, the values of the

FWHM increase from 0.31 for the Ni seed layer film to 0.35 for the film with an Ir seed layer, then inversely reach 0.28 for the Au seed layer film. Obviously, the value of the no-seed layer film becomes about 1.4 times larger than that of the Au seed layer film. The smaller FWHM of the magnetic layer can be caused either by the reduction in defects and/or internal stress or by the increased crystallite size of the film or both of the reasons above.[15] In Fig. 3, we present the images of the morphology of the CoIr films with Au and Ni seed layers from TEM measurements. For the Au seed layer film, the grain size is uniform and grain boundaries are distinct, whereas the size of the crystallization areas is uneven and there are no clear boundaries for the Ni seed layer film. Significantly, the figure showing the Ni seed layer film reveals the mixing of crystallite regions and amorphous regions, which provides an explanation for the large peak intensity ratio. Moreover, Co and Ir atoms may reside at the interstitial site or fill in the interspace between individual grains, which may lead to an increase in defects and/or internal stress.

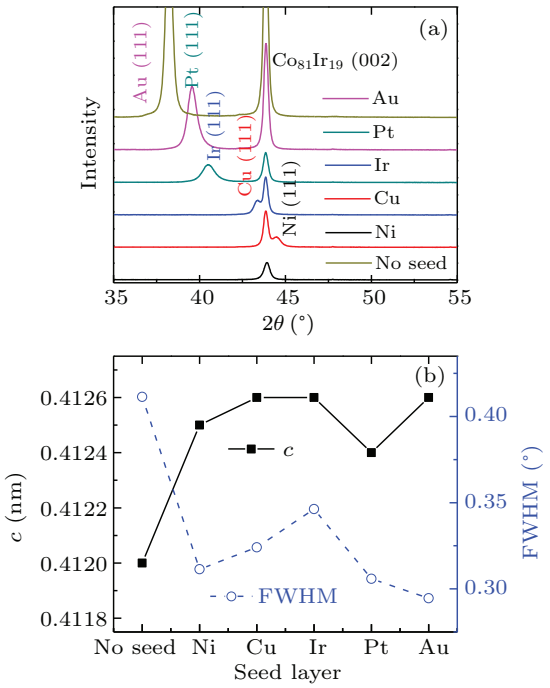


Fig. 2. (a) XRD patterns of the oriented hcp-$Co_{81}Ir_{19}$ films with different seed layers. (b) Lattice parameters c and FWHM, obtained by fitting the CoIr (002) peak shown in panel (a), with different seed layers.

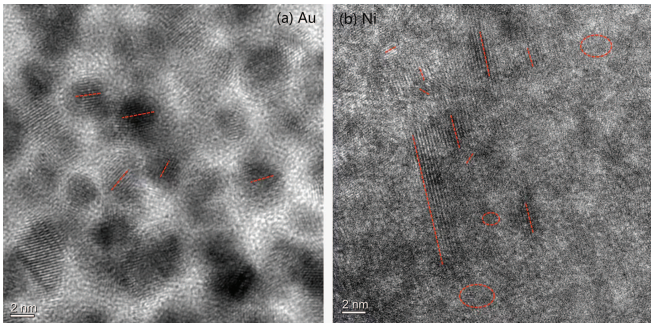


Fig. 3. Images of the morphology of the CoIr films with Au and Ni seed layers, respectively.

The in-plane magnetic hysteresis loops of all the films are shown in Fig. 4(a). These loops were measured with the applied magnetic field parallel to the easy axis during measurements. The remanence ratios of all loops are above 0.92 and the nearly rectangular loops are clearly observed. Furthermore, the determined saturation magnetization $4\pi M_s$ and coercivity H_c from the above hysteresis measurements are plotted in Fig. 4(b). There are no obvious changes in $4\pi M_s$ about 12.4 kOe for the CoIr magnetic layer, which agrees well with reported values.[7] For the Ni seed layer film, $4\pi M_s$ of only the CoIr magnetic layer is 12.8 kOe as shown in Fig. 4(b), whereas the saturation magnetization containing both a Ni seed layer and CoIr layer is about 10.7 kOe. With increasing the lattice mismatch ratio, H_c increases from 54.9 Oe for the Ni seed layer film to 74.3 Oe for the film with a Cu seed layer, then decreases gradually to 27.4 Oe. The reduction in coercivity can be linked drastically to the reduction of defects and/or internal stress,[16] the reduction of the crystallite size, and the increase in exchange coupling between the crystallites.[17] Considering that the tendency of H_c is similar to that of the FWHM with the lattice mismatch ratio, we speculate that the main reason for the change in H_c and FWHM is the same. As is known, the change in crystallite size may cause the opposite tendency of the FWHM and coercivity. Therefore, the change in H_c and FWHM may be mainly attributed to the reduction of defects and/or internal stress with the lattice mismatch ratio. For the film without seed layer, the value remarkably reaches 103.5 Oe about 3.8 times larger than the smallest one. This very large value may come from many defects and/or strong internal stress and/or the large in-plane component of the magnetocrystalline anisotropy field.

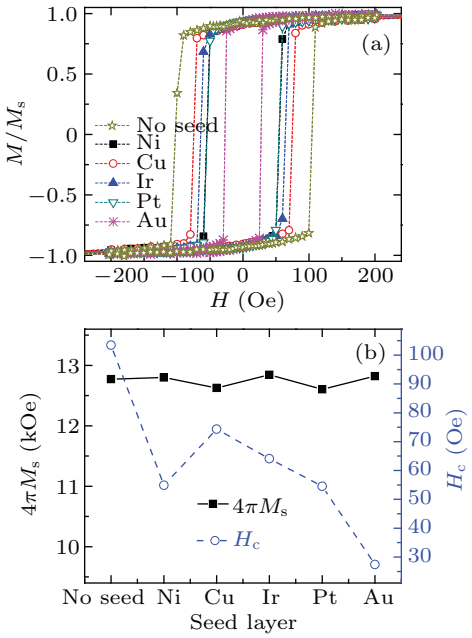


Fig. 4. (a) Normalized in-plane magnetic hysteresis loops of the oriented hcp-$Co_{81}Ir_{19}$ films with different seed layers. (b) The seed layer dependence of the determined $4\pi M_s$ and H_c for the oriented hcp-$Co_{81}Ir_{19}$ films.

As emphasized in our earlier work,[6] we now investigate the magnetic anisotropy properties of our films using ESR measurements. The resonance fields were measured with an external magnetic field applied to the film plane. The microwave magnetic field of about 9 GHz was applied perpendicular to the film plane. As shown in Figs. 5(a)–5(f), the resonance fields of all films display a well-defined in-plane uniaxial symmetry as a function of field orientation ϕ_H, suggesting the samples have an in-plane uniaxial anisotropy.[18] The uniaxial anisotropy is induced by the slight oblique deposition angle, and can be explained within the framework of the so-called self-shadowing model.[19] Taking H_u and H_θ as adjustable parameters, we fitted the experimental data by the following equations:[20]

$$\left(\frac{\omega}{\gamma}\right)^2 = \left[H_\theta + H_u\cos^2\phi_0 + H_r\cos(\phi_0-\phi_H)\right] \times \left[H_u\cos(2\phi_0) + H_r\cos(\phi_0-\phi_H)\right],$$
$$2H_r\sin(\phi_0-\phi_H) = H_u\sin 2\phi_0, \quad (2)$$

where H_θ is the total effective out-of-plane anisotropy field, H_r is the resonance field, ϕ_0 is the value of ϕ_M with the equilibrium positions, ω is the angular frequency of about 18π, and γ is the gyromagnetic ratio. The fitted results are consistent in the measured datum and drawn in Figs. 5(a)–5(f) as black solid lines. The extracted in-plane uniaxial anisotropy fields H_u are shown in Fig. 5(g) as open black squares. Obviously, H_u changes slightly around 18 Oe because of the slight oblique deposition angle. For H_θ shown in Fig. 5(h), the deduced values increase from 10.9–26 kOe with the lattice mismatch ratio, whereas they reduce to 23.2 kOe for the film without a seed layer. For the Ni seed layer film, the corrected H_θ is 11.6 kOe when the perpendicular anisotropy of the Ni seed layer is eliminated. According to the equations $H_\theta = 4\pi M_s - H_{grain}$ and $H_{grain} = 2K_{grain}/M_s$, the calculated K_{grain} is shown in Fig. 5(i). The values are all negative and different from each other, suggesting that K_{grain} is affected by a seed layer and the seed layer material.

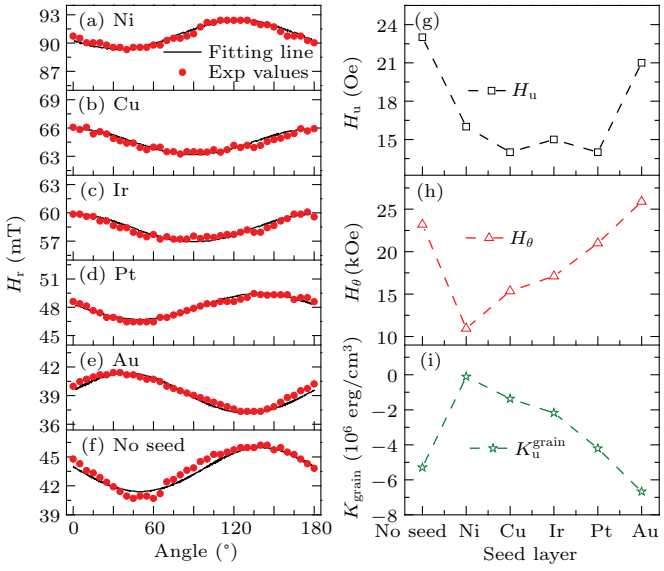


Fig. 5. (a)–(f) Angle dependence of the in-plane resonance field for the oriented hcp-$Co_{81}Ir_{19}$ films with different seed layers. The black solid lines denote the theoretical fits to the experimental datum represented by red dots. (g) The determined in-plane anisotropy field H_u, (h) the total effective out-of-plane anisotropy field H_θ, (i) the deduced magnetocrystalline anisotropy constant K_{grain} as a function of the lattice mismatch ratios for different seed layers.

According to the reported literature,[21,22] K_{grain} is sensitive to the lattice geometry and microstructure, which is restricted by the growth mode of the magnetic layer. The growth modes are mainly governed by the seed-layer surface-free energy γ_s, the magnetic layer surface free energy γ_f, the strain energy γ_e, and the interface energy γ_i.[23] Except for Ir (3.231 J·m^{-2}), the surface free energies of Ni (2.364 J·m^{-2}), Cu (1.934 J·m^{-2}), Pt (2.691 J·m^{-2}), Au (1.626 J·m^{-2}), and Ti (2.570 J·m^{-2}) are smaller than that of Co (2.709 J·m^{-2}).[24,25] As the Ir atomic diameter is bigger than that of Co, the lattice constant of the hcp-CoIr phase becomes bigger with the increase in Ir. We speculate that the surface-free energy of Co is smaller than that of CoIr. Furthermore, the γ_s for the Ni, Cu, Pt, an Au seed layer and Ti amorphous layer is smaller than the γ_f of the CoIr magnetic layer, whereas the γ_s of Ir may be slightly greater than the γ_f of the CoIr layer. Again taking γ_i and γ_e into consideration, it is easy to satisfy the relationship $\gamma_s - \gamma_f - \gamma_e - \gamma_i < 0$. Therefore, the deposited magnetic layer forms three-dimensional islands or clusters at the initial stage, then the following growth has the trend of random orientation distribution and rough surface. As reported in the literature,[26] defects and/or internal stress and/or dislocations may appear at the interface. However, with increasing the lattice mismatch ratio, the mismatch strain between the seed layer and the magnetic layer varies from compressive stress to tensile stress, and tensile stress gradually becomes larger. In order to relieve the mismatch strain, the degree of the orientation of the hcp-CoIr grains may be improved, the microstructure and appearance may be changed, the defects and/or internal stress may be reduced, the crystallite width may be refined, and dislocations may be decreased. We find that the main contribution is both the increasing degree of orientation and the reduction in defects and/or internal stress so that it is consistent with the reason for decreased H_c and FWHM values. The reduced strain energy γ_e is favorable to the layer-by-layer growth of the magnetic layer. During the growth process, the layer-by-layer growth is conducive to improving the degree of the orientation and to reducing the defects and/or internal stress;[27] hence, a smaller K_{grain} is obtained. Apart from these, the different stacking structure ratios and crystallinity and atomic site ordering can also be linked drastically to K_{grain}.[21] For the Ni seed layer film, amorphous regions appear as shown in Fig. 3. And it is difficult to form the hcp-CoIr phase with an easy plane and to improve the degree of orientation because the Ni (111) direction perpendicular to the film plane is an easy axis of mag-

netization; thus, $K_{\rm grain}$ is approximately zero. Despite easily forming hcp stacking, the film without a seed layer has much more random orientation grains and defects, holes, and grain boundaries because of the three-dimensional islands' growth and un-epitaxial growth.[28] Besides, the different seed layer metals have different seed layer thickness ranges, which yield the highly c-axis oriented hcp-(CoIr) films.[29] The seed layer thickness of about 25 nm is optimal for Au metal, whereas the range of the thickness of other metals is not discussed. The other seed layer fixed at 25 nm thickness may be not conducive to the realization of the c-axis oriented growth and hcp stacking. Therefore, the Au seed layer film has the minimum $K_{\rm grain}$ of about -5.299×10^{6} erg·cm^{-3}.

With parameters determined from the VSM and ESR measurements, the high-frequency properties are determined according to Eq. (1). Due to small in-plane uniaxial anisotropy fields $H_{\rm u}$, we calculated the initial permeability $\mu_{\rm i}^{\rm calc}$ and the resonance frequency $f_{\rm r}^{\rm calc}$ with the in-plane anisotropy field equaling $H_{\rm u}$ plus a 200 Oe applied field, as presented in Figs. 6(g) and 6(h). To verify the obtained high-frequency parameters and research the damping constant, we measured the microwave permeability spectra of our SMTFs by VNA with a 200 Oe field applied along the easy axis. Figures 6(a)–6(e) show the real and imaginary parts of the measured complex permeability spectra. The determined $\mu_{\rm i}^{\rm exp}$ and $f_{\rm r}^{\rm exp}$ from the measured spectra are plotted in Figs. 6(g) and 6(h) together with the calculated values. With the different seed layers, the change in the initial permeability is not obvious as shown in Fig. 6(g). The average value is about 58.1 and 59.8 for the calculated values and experimental values, respectively. Almost no changes in the initial permeability are associated with the steady $4\pi M_{\rm s}$ and the nearly invariable in-plane anisotropy field. For the Ni seed layer, the smaller initial permeability results from the smaller saturation magnetization. The $f_{\rm r}^{\rm exp}$ follows the same trend as that of the calculated $f_{\rm r}^{\rm calc}$ with different seed layers. This tendency can be understood by the change in H_θ, which has a direct relation to $K_{\rm grain}$.

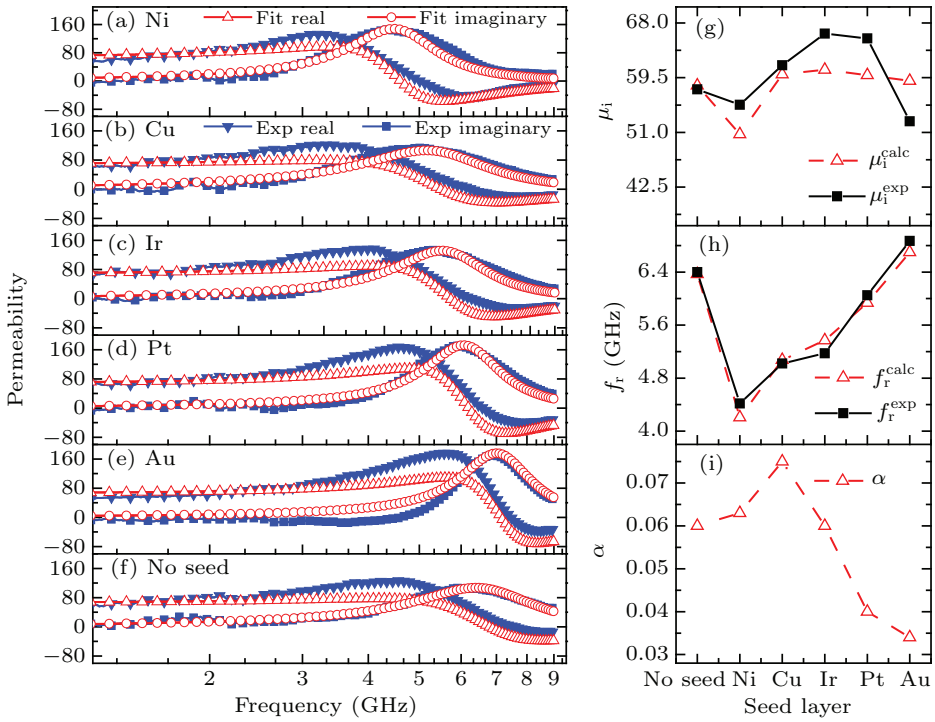


Fig. 6. (a)–(f) Permeability spectra of the oriented hcp-$Co_{81}Ir_{19}$ films with different seed layers. (g) The initial permeability $\mu_{\rm i}$, (h) the natural resonance frequency $f_{\rm r}$, (i) the derived damping constant α for different seed layers. The $\mu_{\rm i}^{\rm exp}$ and $f_{\rm r}^{\rm exp}$ shown as solid black squares are determined from the measured spectra. The calculated values using the determined $4\pi M_{\rm s}$ and the in-plane anisotropy field from the VSM and ESR measurements are also shown for comparison.

In high-frequency applications, the dimensionless damping constant α is one of the key parameters of ultra-high frequency devices.[30] Restricted by the damping constant, the complex permeability spectra can be described by the following formula deduced from the Landau–Lifshitz–Gilbert (LLG) equation[31]

$$\mu = 1 + 4\pi M_{\rm s}\gamma \frac{\omega_1 + {\rm i}\alpha\omega}{\omega_1\omega_2 - \omega^2 + {\rm i}\alpha\omega(\omega_1+\omega_2)}, \qquad (3)$$

in which $\omega_1 = \gamma(4\pi M_{\rm s} - H_{\rm grain} + H_{\rm u}) = \gamma(H_\theta + H_{\rm u})$, $\omega_2 = \gamma H_{\rm u}$, where ω is the angular frequency and α is the damping constant. Using the in-plane anisotropy field and α as the free fitting parameters, we fitted the experimental curves by Eq. (3) as shown in Figs. 6(a)–6(f). The extracted in-plane anisotropy fields are 221 Oe, 220 Oe, 220 Oe, 220 Oe, 228 Oe, and 231 Oe for the Ni, Cu, Ir, Pt, Au, and no seed layer films, respectively. These values are very close to the extracted $H_{\rm u}$ plus 200 Oe applied field. As given in Fig. 6(i), the obtained αincreases from 0.063 for the Ni seed layer film to 0.075 for

the film with a Cu seed layer, then decreases gradually to 0.034 for the Au seed layer film. However, the value of the no seed layer film reaches 0.06, which is about 1.76 times larger than the smallest one. It is well known that the damping constant consists of two parts, namely, the intrinsic and extrinsic contributions. The intrinsic part largely depends on fundamental properties such as M_s and the spin–orbit coupling effect.[11,32] As M_s is extremely close to a constant except for in the Ni seed layer film, this part has no influence on α. With the same origin in spin–orbit coupling,[33] the serious fluctuation in K_{grain} indicates that α is subject to variation. In general, there is no linear relationship between K_{grain} and α. Besides, the extrinsic part is generally explained by the defect-induced two magnon model and/or the local resonance model,[34] both of which are associated with magnetic inhomogeneities within the material (e.g., due to anisotropy dispersion and surface or interface roughness). As mentioned above, the improved orientation in the grains and the reduced defects and/or internal stress result in the decrease in magnetic inhomogeneities. With increasing the lattice mismatch ratio, a decreasing trend is shown in both FWHM and α, while the discrepancy is also obvious. Therefore, the extrinsic part plays a vital role in the variation in α, and the intrinsic part is also a supplemental factor. Interestingly, because of the smallest extrinsic part, the minimum of α is inevitable for the Au seed layer film.

4. Conclusion

In summary, *c*-axis oriented hcp-$Co_{81}Ir_{19}$ magnetic films were successfully prepared on different seed layers (Ni, Cu, Ir, Pt, Au, and no seed), and were investigated thoroughly by different measurement techniques. The orientation and defects of the *c*-axis oriented hcp-(CoIr) grains are strongly affected by the seed layer. The coercivity H_c and K_{grain} are strongly dependent on the seed layer and seed layer material. While the determined saturation magnetization $4\pi M_s$ and in-plane uniaxial anisotropy fields H_u are independent of the lattice parameters, microstructure, and material of the seed layer. As expected, the initial permeability has little relation to the seed layer, while the natural resonance frequency is strongly restricted through K_{grain} affected by the lattice mismatch ratio. The extracted lower α is relative to the improved grain orientation and the reduced defects and/or internal stress. Among all the films, the film for the Au seed layer has the optimal performance of soft magnetic properties and microwave properties. We expect that these results can further help us improve the static and dynamic frequency properties for further applications.

Acknowledgements

Project supported by the Natural Science Foundation of Ningxia in China (Grant No. 2022AAC03288) and the Ningxia New Solid Electronic Materials and Devices Research and Development Innovation Team (Grant No. 2020CXTDLX12).

References

[1] Yang X, Wei J Q, Li X H, Gong L Q, Wang T and Li F S 2012 *Phys. B* **407** 555
[2] Yamaguchi M, Miyazawa Y, Kaminishi K, Kikuchi H, Yabukami S, Arai K I and Suzuki T 2004 *J. Magn. Magn. Mater.* **268** 170
[3] Klemmer T J, Ellis K A, Chen L H, van Dover B and Jin S 2000 *J. Appl. Phys.* **87** 830
[4] Wang F, Inoue A, Han Y, Zhu S L, Kong F L, Zanaeva E, Liu G D, Shalaan E, Al-Marzouki F and Obaid A 2017 *J. Alloys Compd.* **723** 376
[5] Xue D S, Li F S, Fan X L and Wen F S 2008 *Chin. Phys. Lett.* **25** 4120
[6] Wang T, Wang Y, Tan G G, Li F S and Ishio S 2013 *Phys. B* **417** 24
[7] Zhang S, Zhang C H, Ma L, Ma T Y, Wang T, Gao M Z and Li F S 2022 *Phys. B* **638** 413846
[8] Chen S C, Jen S U, Chen R Z, Lu C F, Wang C M and Kuo P C 2018 *J. Magn. Magn. Mater.* **459** 106
[9] Fu Y, Miyao T, Cao J W, Yang Z, Matsumoto M, Liu X X and Morisako A 2007 *J. Magn. Magn. Mater.* **308** 165
[10] Akansel S, Venugopal V A, Kumar A, Gupta R, Brucas R, George S, Neagu A, Tai C W, Gubbins M, Andersson G and Svedlindh P 2018 *J. Phys. D: Appl. Phys.* **51** 305001
[11] Wu S, Smith DA, Nakarmi P, Rai A, Clavel M, Hudait MK, Zhao J, Marc MF, Mewes C, Mewes T and Emori S 2022 *Phys. Rev. B* **105** 174408
[12] Ma T Y, Luo Z, Li Z W, Qiao L, Wang T and Li F S 2019 *Chin. Phys. B* **28** 057505
[13] Morris R A, Inaba Y, Harrell J W and Thompson G B 2010 *Thin Solid Films* **518** 4970
[14] Chen S C, Jen S U, Chen R Z, Lu C F, Wang C M and Kuo P C 2018 *J. Magn. Magn. Mater.* **459** 106
[15] Liu C M, Xing X, Zhang Y, Jiang Y and Zu X T 2011 *Chin. Phys. Lett.* **28** 127201
[16] Morris R A, Inaba Y, Harrell J W and Thompson G B 2010 *Thin Solid Films* **518** 4970
[17] Feng E X, Wang Z K, Du H W, Wei J W, Cao D R, Liu Q F and Wang J B 2014 *J. Appl. Phys.* **115** 17A307
[18] Chakraborty A, Khan A, Dutta P and Seehra M S 2008 *Mater. Lett.* **62** 970
[19] Lou J, Insignares R E, Cai Z, Ziemer K S, Liu M and Sun N X 2007 *Appl. Phys. Lett.* **91** 182504
[20] Ma T Y, Jiao J Y, Li Z W, Qiao L, Wang T and Li F S 2018 *Appl. Surf. Sci.* **457** 598
[21] Zhang S, Pang H, Hai L, Li W Y, Wang T and Li F S 2019 *J. Appl. Phys.* **126** 083907
[22] Wei X P, Cao T Y, Sun X W, Gao Q, Gao P F, Gao Z L and Tao X M 2020 *Chin. Phys. B* **29** 077105
[23] Kitakami O, Okamoto S and Shimada Y 1996 *J. Appl. Phys.* **79** 6880
[24] Mezey L Z and Giber J 1982 *Jpn. J. Appl. Phys.* **21** 1569
[25] Yan H L, Yan J L and Zhao G 2019 *Chin. Phys. B* **28** 114401
[26] Smith D J, Modak A R, Rabedeau T A and Parkin S S P 1997 *Appl. Phys. Lett.* **71** 1480
[27] Hayashi N, Miyamoto Y, Machida K and Tamaki T 2005 *J. Magn. Magn. Mater.* **287** 387
[28] Morris R A, Inaba Y, Harrell J W and Thompson G B 2010 *Thin Solid Films* **518** 4970
[29] Zhang L N, Hu J F, Chen J S and Ding J 2009 *J. Appl. Phys.* **105** 07A743
[30] Kalarickal S S, Krivosik P, Das J, Kim K S and Patton C E 2008 *Phys. Rev. B* **77** 054427
[31] Phuoc N N, Xu F and Ong C K 2009 *J. Appl. Phys.* **105** 113926
[32] Kambersky V 1970 *Can. J. Phys. B* **48** 2906
[33] He P, Ma X, Zhang J W, Zhao H B, Lupke G, Shi Z and Zhou S M 2013 *Phys. Rev. Lett.* **110** 077203
[34] Arias R and Mills D L 1999 *Phys. Rev. B* **60** 7395